

Article

Kinetic Investigation of the Deep Desulfurization of 5 wt% Si High-Silicon Austenitic Stainless Steel

Guanxiong Dou ^{1,2}, Hanjie Guo ^{1,2,*}, Jing Guo ^{1,2,*} and Xuecheng Peng ^{1,2}

¹ School of Metallurgical and Ecological Engineering, University of Science and Technology Beijing (USTB), Beijing 100083, China; douguanxiong430@gmail.com (G.D.); pxcustb@163.com (X.P.)

² Beijing Key Laboratory of Special Melting and Preparation of High-End Metal Materials, Beijing 100083, China

* Correspondence: guohanjie@ustb.edu.cn (H.G.); guojing@ustb.edu.cn (J.G.)

Abstract: Given the demand for extremely low sulfur content in 5 wt% Si high-silicon austenitic stainless steel (SS-5Si), smelting utilizes a slag composition of CaF₂-CaO-Al₂O₃-MgO-SiO₂ with a basicity of 1 to 3, Al₂O₃ content ranging from 2.04 to 9.61%, and CaF₂ content between 20.8 and 31.62%. Experiments designed to investigate the sulfur content in molten steel at temperatures of 1773 K, 1823 K, and 1873 K over durations of 1, 5, 10, 15, and 30 min, under varying slag compositions, corroborated with a theoretically derived model hypothesizing a “rate-controlling” step in mass transfer, revealed that the mass transfer of sulfur within the molten steel was determined to be the rate-controlling step (RCS) in the (CaO) + [S] = (CaS) + [O] reaction kinetics, and the variability of the mass transfer coefficient of sulfur, $k_{S,m}$, in the molten steel ranged from $1.04 \times 10^{-5} \text{ m}\cdot\text{s}^{-1}$ to $2.24 \times 10^{-5} \text{ m}\cdot\text{s}^{-1}$. Based on the temperature dependency of $k_{S,m}$, the apparent activation energy for the desulfurization reaction was estimated to be 96.03 kJ/mol. Considering the slag components, the binary basicity, denoted as R , exerted an overriding influence on the process of desulfurization. At a basicity of 1, the sulfur content within the liquid steel was reduced, from 22 ppm to 11 ppm within a time span of 30 min. In contrast, an increase in the basicity to a value of 3 showed a significant consequence: over an identical temporal duration of 30 min, the sulfur content was drastically reduced to 2.2 ppm. By contrast, an initial surge in desulfurization rates is observed within the first five minutes, attributable to relatively lower concentrations of Al₂O₃ and higher levels of CaF₂. Subsequently, these parameters exert no significant influence on the kinetics of the desulfurization process.



Citation: Dou, G.; Guo, H.; Guo, J.; Peng, X. Kinetic Investigation of the Deep Desulfurization of 5 wt% Si High-Silicon Austenitic Stainless Steel. *Processes* **2024**, *12*, 781. <https://doi.org/10.3390/pr12040781>

Academic Editor: Liming Lu

Received: 8 March 2024

Revised: 3 April 2024

Accepted: 6 April 2024

Published: 12 April 2024



Copyright: © 2024 by the authors. Licensee MDPI, Basel, Switzerland. This article is an open access article distributed under the terms and conditions of the Creative Commons Attribution (CC BY) license (<https://creativecommons.org/licenses/by/4.0/>).

Keywords: slag-steel reaction; kinetics; rate-controlling step; deep desulfurization; transfer coefficient

1. Introduction

High-silicon-containing stainless steels (generally surpassing 4 wt%) exhibit remarkable corrosion resistance, particularly in environments containing hot concentrated sulfuric acid [1–3]. This characteristic promotes their extensive application in sectors such as sulfuric acid processing and chemical fertilizer production [4,5]. The sulfur content plays a pivotal role in determining the quality of steel, as it fosters the emergence of sulfide inclusions that serve as harmful impurities [6–8]. Over time, inclusions erode the integral properties of steel, such as its strength, corrosion resistance, and surface finish [9–13]. In corrosive environments, steel’s sulfide inclusions corrode and dissolve before the metal matrix itself [14,15]. Research by Shibaeva et al. on the corrosion impact of varying sulfur contents of API-5 L X60-X100 low-carbon steel elucidated several key findings [16]. Sulfide inclusions were found to exacerbate the corrosion current, with higher sulfur content inversely proportional to the steel’s passivation, thereby narrowing the range of passive state potentials. For 316L stainless steel (SS), Chen et al. found a direct correlation between increased sulfur content and an escalating grade and proportion of sulfides [17]. Simultaneously, the sulfide distribution became increasingly dense, accelerating the rate of pitting

corrosion weight loss. Concurrently, Li et al. determined that sulfides not only facilitated pitting but also contributed to the slight dissolution of oxides. Their microelectrochemical analysis emphasized the evident impact of both MnS and oxy-sulfide eliminations on the 304 SS matrix, thereby heightening the substrate's susceptibility to pitting corrosion [18]. Hence, reducing sulfur content in steel is essential for maintaining its quality and durability.

A universal agreement among scholars is that lessening the harmful sulfur content in steel results in a reduction in sulfide levels, thereby substantially amplifying its inherent corrosion-resistant attributes. Wilde et al. [19] examined the effect of sulfur content, varying from 80 to 1700 ppm, on the corrosion resistance of austenitic stainless steel (14 wt% Cr-14 wt% Ni) across a spectrum of environments. They found that a decrease in sulfur content from 1700 ppm to 80 ppm resulted in a reduction in the anodic dissolution rate by a factor of seven. Electrochemical polarization data extrapolated a clear correlation between elevated sulfur content and an increase in the exchange current density for metal dissolution, consequently accelerating anodic dissolution. Simultaneously, Wan et al. [20] performed a comprehensive study on the corrosion resistance and pitting behavior at various sulfur content levels in free-cutting austenitic stainless steel, via an electrochemical workstation and scanning electron microscope. Their results showed a significant reduction in the corrosion rate from 10.55 to 2.83 $\mu\text{m}/\text{a}$, coinciding with a drop in the sulfur content in the steel from 0.270% to 0.089%. Further investigation into the corrosion resistance of 17-4 PH stainless steel, fabricated via selective laser melting, showed that the re-austenitized SLMed steel ($w[\text{S}]_{\%} = 0.003$) exhibited superior general corrosion resistance compared to its wrought counterpart ($w[\text{S}]_{\%} = 0.02$). This result was attributed to the diminished sulfur content, particularly to the lower MnS inclusion content, in the re-austenitized SLMed steel. In contrast, in wrought steel, the dissolution of MnS inclusions caused the formation of a sulfur-rich layer in the proximate regions, thereby prompting the destabilization of the passive film and subsequently, the deterioration of the general corrosion resistance [21]. Refined slag significantly impacts steel cleanliness. Good refining slag is primarily characterized by a high melting rate, good fluidity, strong inclusion adsorption, and excellent desulfurization capability.

In the desulfurization process of steelmaking, by improving the composition of refining slag, the activity of the resulting desulfurization products can be reduced, and the capacity of slag sulfides can be enhanced, thereby increasing the efficiency of these processes. Building on Wagner's [22] coexistence theory model, Zhang [23] proposed a slag molecular ion coexistence model. By employing thermodynamic principles, the model calculates the concentration of each unit to characterize the activity of each component, yielding results consistent with reality. Based on Zhang's model, Lin and colleagues [24] predicted the activity of SiO_2 at 1600 °C. The model's predicted SiO_2 activity values align closely with data reported in the literature, highlighting the significance of accurately predicting the activity of each component in slag for refining process improvement. Subsequently, metallurgists developed models such as KTH and optical basicity based on the activity of slag to predict the relationship between sulfide capacity and slag composition [25–31]. While there are discrepancies in their forecasts, Li [32] utilized the two referenced models to conduct a statistical validation of the sulfide capacity predictions for the $\text{CaO-SiO}_2\text{-MgO-Al}_2\text{O}_3\text{-Fe}_x\text{O}$ slag system at 1500 °C. Concurrently, Wang and colleagues provided experimental corroboration for these predictions [33]. It was observed that both the KTH and optical basicity models' forecasts closely mirrored actual measurements, with the KTH model's predictions notably aligning more precisely with the experimental outcomes. From a theoretical basis, however, the predictions of any model come with a certain degree of error and are not applicable under all working conditions of the production process. Lv [34] adjusted the desulfurization model of LF refining slag according to the actual situation, achieving an accuracy where the sulfur content prediction error was within 0.003% (mass percentage) for 84% of the cases. In recent years, there has been some research progress in refining slag. Although models can predict the performance of the refining slag system, studies on reducing the sulfur content in molten steel to below 5 ppm are

scarce, and the accuracy of the predicted activity and sulfide capacity models still needs further optimization. Moreover, during the desulfurization process, how to maintain the uniformity of sulfur has always been a challenging topic in the study of kinetics.

To address the prevailing challenges, our study examines the kinetics associated with desulfurization, using the $\text{CaF}_2\text{-CaO-Al}_2\text{O}_3\text{-MgO-SiO}_2$ slag system. This study builds upon our seminal work investigating the thermodynamics and kinetics of deep deoxygenation in SS-5Si [35]. The study aims to determine the variables that can accommodate desulfurization to approximately 5 ppm. Moreover, a precise kinetic model has been developed to capture the deep desulfurization process and determine the inherent correlation between the process and deoxygenation. The insights derived from this study are expected to enhance the theoretical foundation for large-scale production.

2. Experimental Design and Procedure for the Assessment of the Deep Desulfurization Kinetics of SS-5Si

2.1. Theoretical Basis for the Study of Deep Desulfurization Kinetics

In molten steel environments, sulfur has minimal solubility within the austenitic framework at reduced temperatures. Upon solidification, sulfur primarily forms precipitates at the grain boundaries, mainly as sulfides. An increase in the sulfur concentration within the steel invariably augments sulfide segregation at these intergranular boundaries, a phenomenon that adversely impacts the resistance to the corrosion of steels [36–38]. Consequently, the stringent modulation of sulfur content in molten steel is imperative. During the metallurgical processes, achieving sulfur removal from the steel via slag–steel interactions is paramount. Furthermore, identifying apt slag constituents for efficacious desulfurization and delving into the associated desulfurization kinetics are requisite endeavors.

In practical manufacturing processes, to achieve an ultralow sulfur content (below 0.001%) in SS-5Si steel, the appropriate slag composition based on prior thermodynamic models is imperative to determine [35].



From Equations (1) and (2), the activities of (CaO), (CaS), (MgO), and (MgS) within the slag greatly influence the desulfurization process in tandem with the variations in dissolved oxygen [O] within the molten steel. Concerning SS-5Si, the equilibrium sulfur content ($w[\text{S}]_{\%}$) in the liquid steel, in conjunction with the $\text{CaF}_2\text{-CaO-Al}_2\text{O}_3\text{-MgO-SiO}_2$ slag reaction [38], elucidates the interrelationship between the reactive chemical constituents in the steel and variables such as temperature, as delineated by Equations (3) and (4).

$$\lg w[\text{S}]_{\%,\text{CaO}} = \left\{ \lg a_{\text{CaS}} + \lg f_{\text{O}} + \lg w[\text{O}]_{\%} - \lg f_{\text{S}} - \lg a_{\text{CaO}} - \left(-\frac{5525.8}{T} + 1.50 \right) \right\} \quad (3)$$

$$\lg w[\text{S}]_{\%,\text{MgO}} = \left\{ \lg a_{\text{MgS}} + \lg f_{\text{O}} + \lg w[\text{O}]_{\%} - \lg f_{\text{S}} - \lg a_{\text{MgO}} - \left(-\frac{10635.6}{T} + 1.83 \right) \right\} \quad (4)$$

During steelmaking, the equilibrium sulfur partition ratio between slag and metal, denoted as $L_s = (\text{pct S})/[\text{pct S}]$, can be thermodynamically elucidated as an indicator of the slag's desulfurization efficiency [39–41]. Notable studies by Yang [42], Shi [43], and Duan [44] have consistently ascertained that the desulfurization efficacy of MgO in the slag, when juxtaposed with CaO, is negligible, rendering Equation (4) superfluous; thus, for computational rigor, only Equation (3) warrants consideration. As inferred from Equations (1) and (3), the ultralow oxygen content in molten steel emerges as the paramount parameter ensuring exceedingly low sulfur levels [45]. To ascertain the sulfur content at the slag–metal equilibrium, the ensuing parameters must be accurately calculated:

1. The activity of the pertinent components (a_{CaO} , a_{MgO}) within the slag matrix can be ascertained utilizing the ion–molecule coexistence theory (IMCT) framework [42].
2. The activity coefficients, denoted as $f_{\%,i}$, for [S] and [O] in the SS-5Si steel composition delineated in Table 1 across diverse reaction temperature spectra need to be computed. The coefficients delineating activity interactions used in this study are provided in Table 2.
3. Based on the sophisticated thermodynamic model elucidating the ultralow oxygen content equilibrium between [Si] and [O] within the steel’s molten phase, an in-depth investigation into the reactive behavior of SS-5Si molten steel when interfaced with CaF_2 -CaO- Al_2O_3 -MgO-SiO₂ slag was performed. The consequent findings, consisting of the equilibrium oxygen content within the molten steel under an assortment of reactive conditions (when [Si]-[O] reaction are at equilibrium), computed and verified via rigorous experimental results [35].

Table 1. Chemical composition of the molten metal used in the study (Weight Percent) [35].

| C | Si | Mn | Al | Mo | Cr | Ni | Cu | O | S | N | Fe |
|------|----|------|-----|------|-------|------|------|--------|--------|------|------|
| 0.02 | 5 | 0.49 | 0.1 | 1.13 | 12.95 | 18.3 | 1.05 | 0.0025 | 0.0022 | 0.01 | Bal. |

Table 2. Interaction coefficients used in the present study.

| e_i^j | C | Si | Mn | Al | Mo | Ni | Cr | O | S |
|---------|-------|--------|--------|-------|--------|-------|-------|-------|--------|
| O | −0.45 | −0.131 | −0.021 | −3.9 | 0.0035 | 0.008 | −0.04 | −0.2 | −0.133 |
| S | 0.11 | 0.063 | −0.026 | 0.035 | 0.002 | 0 | −0.01 | −0.27 | −0.028 |

In the context of the interactions between the SS-5Si molten steel and the CaF_2 -CaO- Al_2O_3 -MgO-SiO₂ slag under [Si]-[O] equilibrium, the specific conditions of the slag that dictate the balanced oxygen content in the molten steel were examined. Through these investigations, the corresponding slag compositions were determined. To explore the relationship between $w[S]_{\%}$ in the molten steel, derived from the desulfurization reaction at (CaO)-[S] equilibrium, and its actual content, as well as the interconnections of deoxidation and desulfurization reactions in thermodynamic equilibria, we used the IMCT thermodynamic prediction model, analogous to our prior study [35]. Under conditions where $w(MgO)_{\%} = 10$ and $w(CaF_2)_{\%} = 20$, the influence of Al_2O_3 content (ranging from 1–10%) on $w[S]_{\%}$ in the molten steel at binary basicities of 1, 2, and 3 is shown in Figure 1. Key observations from the calculations used in Figure 1 included the following:

1. At 1873 K, with a basicity of 1, the equilibrium [S] content in the molten steel augments with increasing Al_2O_3 . However, at basicity levels of 2 and 3, the Al_2O_3 content in the slag had negligible influence on this equilibrium. This result effectively aligned with the findings of Zhang et al. [46], who proposed that elevated slag basicity considerably enhanced the purity of Si-Mn-deoxidized 430-grade stainless steel, whereas shifts in the C/A ratio had a minimal effect on purity.
2. Figure 1b depicts our findings from ultralow oxygen experiments on SS-5Si steel [35]. When the Al_2O_3 content in the CaF_2 -CaO- Al_2O_3 -MgO-SiO₂ slag is less than 2.73%, the [Si]-[O] equilibrium reaction controlled the oxygen content in the molten steel. With the basicities of 2 and 3, the resultant minimum equilibrium oxygen contents are 2.89 and 1.5 ppm, respectively, as shown at points M1 and M2. The oxygen content similarly reduced with increasing basicity, consistent with the observed decline of $w[S]_{\%}$ at 1873 K as the binary basicity of the slag increased.
3. Utilizing an analogous thermodynamic model, the observed patterns from the reaction depths of desulfurization and deoxygenation between SS-5Si steel and the slag were extremely similar. Notably, for a greater deoxidation, $w(Al_2O_3)_{\%}$ needs to be approximately less than 2 to achieve an ultralow $w[O]_{\%,Si}$. As per Figure 1a, from a

thermodynamic perspective, achieving ultralow sulfur had a minimal relationship to the $w(\text{Al}_2\text{O}_3)\%$ in slag.

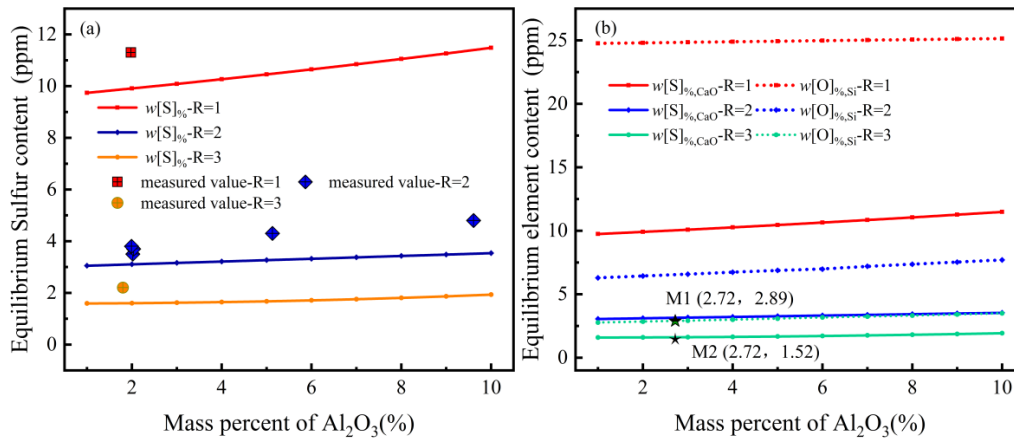


Figure 1. Relationship between the basicity and Al_2O_3 content in the $\text{CaF}_2\text{-CaO-Al}_2\text{O}_3\text{-MgO-SiO}_2$ slag for (a) equilibrium oxygen content, (b) equilibrium oxygen content at 1873 K for SS-5Si.

Figure 1 clearly shows the thermodynamic prerequisites for greater deoxygenation and desulfurization. As illustrated in Figure 1b, under a basicity of 3 and $w(\text{Al}_2\text{O}_3)\%$ of 2.72, the calculations from markers M1 and M2 indicated that $w[\text{O}]_{\%}\text{-Si}$ controlled by the $[\text{Si}]\text{-}[\text{O}]$ equilibrium reaction needed to be 2.89 ppm, with a corresponding $w[\text{S}]_{\%}$ of 1.52 ppm. This result provided the ideal thermodynamic scenario. However, the kinetic practicality of profound desulfurization remained to be determined. To this end, we designed nine distinct slag compositions, encompassing variations in slag basicity (S1–S3), Al_2O_3 content (S4–S6), and CaF_2 content (S7–S9), for experimental laboratory-scale studies with SS-5Si steel. The detailed slag compositions are provided in Table 3.

Table 3. Composition of slag used in this study (Weight Percent).

| Variable | CaO | SiO ₂ | CaF ₂ | MgO | Al ₂ O ₃ |
|--|-------|------------------|------------------|-------|--------------------------------|
| Binary basicity | | | | | |
| S1 | 29.44 | 29.44 | 29.31 | 9.83 | 1.98 |
| S2 | 38.35 | 19.17 | 30.27 | 10.19 | 2.02 |
| S3 | 44.53 | 14.84 | 29.23 | 9.60 | 1.80 |
| Al ₂ O ₃ Content | | | | | |
| S4 | 38.80 | 18.21 | 30.63 | 10.31 | 2.04 |
| S5 | 37.13 | 18.56 | 29.31 | 9.87 | 5.13 |
| S6 | 34.59 | 17.29 | 28.70 | 10.06 | 9.61 |
| CaF ₂ Content | | | | | |
| S7 | 44.73 | 22.37 | 20.87 | 10.04 | 1.99 |
| S8 | 42.21 | 21.11 | 25.33 | 9.47 | 1.88 |
| S9 | 38.64 | 18.14 | 31.23 | 10.08 | 1.91 |

2.2. Experimental Design and Equipment

The SS-5Si steel was fabricated utilizing a sophisticated vacuum induction melting technique, with its specific chemical composition listed in Table 1. The cast ingot, weighing approximately 5 kg and possessing a diameter of approximately 100 mm, underwent homogenization at 1150 °C for 6 h within a resistance furnace, aimed at reducing both micro- and macrosegregation. Subsequently, the sample was precisely hot-forged into bars with a diameter of 50 mm. The chemical composition of the slag is detailed in Table 3. To identify the impact of basicity on the sulfur concentration, a comparative analysis of S1, S2, and S3 was performed. Similarly, the influence of Al_2O_3 content on sulfur concentration was evaluated through S4, S5, and S6, while the influence of CaF_2 content was determined by examining S7, S8, and S9. Notably, the slag was rich in magnesium oxide, ensuring that the integrity of the magnesium oxide crucible was preserved.

Investigations were conducted using a vertical resistance-heated aluminum tube furnace, fortified with MoSi_2 heating elements. Figure 2 illustrates the operational sequence

characteristics of the smelting experiments. The furnace's temperature regulation was accurately managed through a proportional–integral–derivative (PID) controller, conjoined with a type B benchmark thermocouple. As a preliminary measure, an auxiliary type B thermocouple facilitated the thorough calibration of the temperature to a precise 1873 K (1600 °C). Thus, the methodology of the experiment was elucidated:

1. The slag underwent synthesis in a graphite crucible, which featured external dimensions of 50 mm in diameter, 44 mm internally, and a height of 88 mm. This crucible was subsequently placed inside an electric resistance furnace, which operated under a purified argon atmosphere to ensure a uniform temperature distribution. The temperature was progressively increased from ambient conditions to 1873 K, at which it was maintained for 20 min. This procedure was aimed at achieving a homogeneous slag composition.
2. A precisely measured 10 g of premelted slag was introduced into the upper graphite crucible through a small opening at its base. To facilitate the smooth descent of the molten slag into the lower crucible, the inclination of the upper crucible was meticulously adjusted to 110 degrees. A graphite plug, placed at the opening, moderated the interaction between the slag and the steel. After ensuring a consistent surface quality, a 40 g steel specimen was placed in a MgO crucible, which had dimensions of 30 mm external diameter, 25 mm internal diameter, and 35 mm height. To prevent damage to the MgO crucible, it was encased in a graphite crucible with an outer diameter of 36 mm, an inner diameter of 31 mm, and a height of 40 mm. For ease of handling, this assembly was further contained within a larger graphite crucible, measuring 66 mm in outer diameter, 54 mm in inner diameter, and 140 mm in height.
3. Upon attaining a temperature of 1873 K, the bilayer crucible was positioned within an electric resistance furnace, under a purified Ar atmosphere at a flow rate of 2–4 L/min. Concurrently, a transient decline in temperature was observed. Once the thermal equilibrium was re-established at 1873 K, the steel and slag were sustained for a duration of 15 min, ensuring their comprehensive liquescence. Subsequently, the graphite plug was disconnected, initiating the interaction between the slag and steel. This juncture was designated as the inception of the reaction.
4. In periodic intervals (1, 5, 10, 15, and 30 min) after the initiation of the reaction, the entire crucible was quickly removed from the furnace and promptly submerged in an icy water bath. After the culmination of the interaction between the slag and steel, discrete samples were taken, each weighing approximately 1 g. The sulfur quantification within the alloy specimens was accurately measured using a carbon-sulfur analyzer (ELTRA CS-3000) at the National Analysis Center for Iron and Steel (NACIS), China. For each experimental iteration, a minimum of three metallic samples were performed for compositional analysis, with the mean value of these triplicate results representing the sulfur concentration within the ingot.

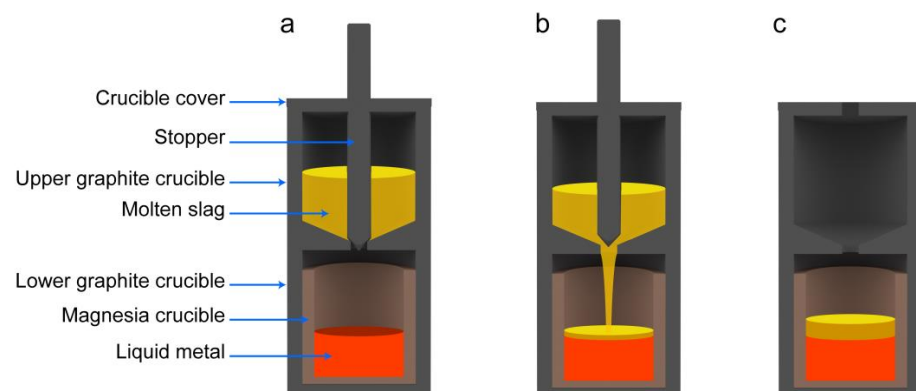


Figure 2. Schematic diagram of the double-layer crucible at different stages: (a) melting process, (b) reaction initiation, and (c) slag–metal reaction.

3. Results

Based on the thermodynamic investigation of the deep desulfurization reaction in SS-5Si, comprehensive laboratory examinations were performed using an array of nine distinct slag compositions in conjunction with SS-5Si steel. Based on the observations from the quantified sulfur concentrations within the molten steel across various temporal reaction intervals (referenced in Tables 3 and 4), a sophisticated kinetic mass transfer model tailored for the (CaO)-[S] desulfurization mechanism was developed. This model was pivotal for delineating the rate-controlling step (RCS) inherent in individual desulfurization reactions, gauging the temporal span necessary for attaining equilibrium in the desulfurization process, and projecting the dynamic sulfur concentration evolution within the liquid steel under an array of kinetic conditions.

Table 4. Sulfur content of the experimental ingots at 1873 K (ppm).

| Variable | 0 min | 1 min | 5 min | 10 min | 15 min | 30 min |
|--|-------|-------|-------|--------|--------|--------|
| Binary basicity | | | | | | |
| S1 | 22 | 18.9 | 16.4 | 13.7 | 12.5 | 11.3 |
| S2 | 22 | 13.7 | 10 | 7.3 | 4.7 | 3.5 |
| S3 | 22 | 12.5 | 8.3 | 5.4 | 3.7 | 2.2 |
| Al ₂ O ₃ Content | | | | | | |
| S4 | 22 | 13 | 9.6 | 6.5 | 4.5 | 3.6 |
| S5 | 22 | 14.6 | 10.4 | 7.3 | 4.8 | 4.3 |
| S6 | 22 | 16.3 | 10.8 | 7.4 | 5.1 | 4.8 |
| CaF ₂ Content | | | | | | |
| S7 | 22 | 14.1 | 10.5 | 6 | 4.7 | 3.8 |
| S8 | 22 | 13 | 10.5 | 5.7 | 4.2 | 3.7 |
| S9 | 22 | 12.7 | 10.1 | 5.4 | 4.2 | 3.6 |

In accordance with the boundary layer theory formulated by Wanger, the reaction regarding the removal of [S] from molten steel in the presence of slag (CaO) can be expressed as follows: (CaO) + [S] = (CaS) + [O]. This intricate reaction mechanism comprises a sequence of five elementary steps:

1. Mass transfer of [S] in the molten steel from the bulk to the slag–metal interface: [S] → [S]^{*};
2. Mass transfer of (CaO) in the molten slag from the bulk to the slag–metal interface: (CaO) → (CaO)^{*};
3. Interface chemical reaction: (CaO)^{*} + [S]^{*} = (CaS)^{*} + [O]^{*};
4. Mass transfer of [O] in the molten steel from the slag–steel interface to the bulk: [O]^{*} → [O];
5. Mass transfer of (CaS) in the molten slag from the slag–steel interface to the bulk: (CaS)^{*} → (CaS)

At elevated temperatures, the rates of interfacial chemical reactions are rapid, implying that step (3) will not act as the rate-controlling step in the reaction kinetics. Whilst the majority of each phase remains consistent in its composition, a discernible concentration gradient manifests adjacent to both facets of the slag–metal interface, particularly for those species for which the RCS is the predominant transport mechanism. Consequently, steps (1), (2), (4), or (5) which pertain to the transference of reactants or products via the concentration boundary layer to or from the slag–metal interface, are the probable RCSs of the reaction at elevated temperatures [47]. In accordance with the five equations delineating heterogeneous reaction kinetics based on the principle of the effective boundary layer [48] as shown in Figure 3, the flux pertaining to component *i* (where *i* encompasses [S], [O], (CaO), and (CaS)) across a given unitary surface is calculated via Equation (5).

$$J_i = \frac{1}{A} \frac{dn_i}{dt} = k_{i,s} (C_{i,s}^* - C_{i,s}^b) = k_{i,m} (C_{i,m}^b - C_{i,m}^*) \left(\text{mol} \cdot \text{m}^{-2} \cdot \text{s}^{-1} \right) \quad (5)$$

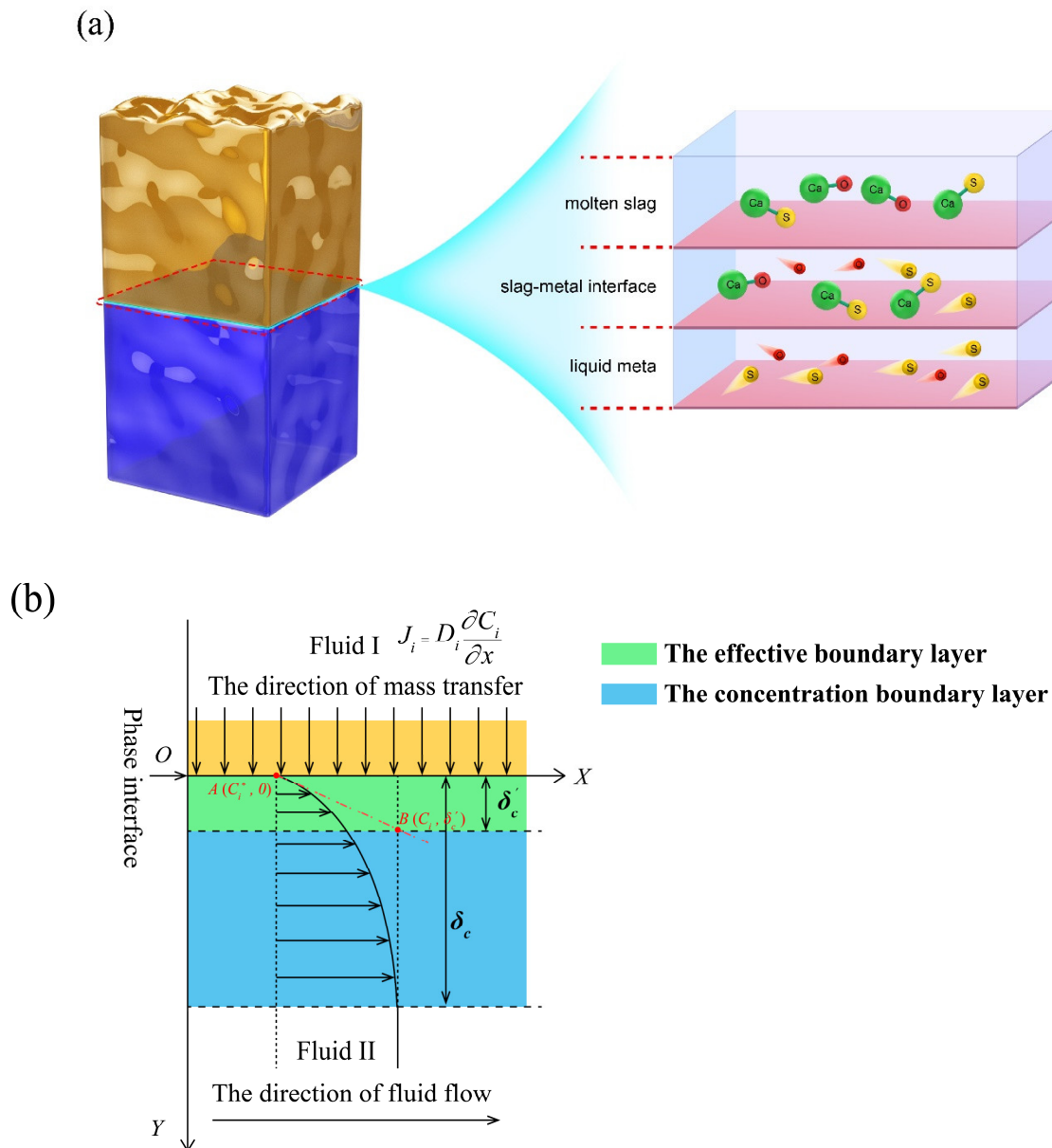


Figure 3. (a) A macroscopic model of heterogeneous reactions; (b) Schematic of the concentration C_i^b distribution during the heterogeneous reaction and the definition of the thickness of the effective boundary layer δ_c' proposed by Wagner.

The parameters J_i , k_i , C_i , and A represent the molar flow ($\text{mol} \cdot \text{m}^{-2} \cdot \text{s}^{-1}$), mass transfer coefficient (m^{-1}), molar concentration of element i within the liquid alloy or slag ($\text{mol} \cdot \text{m}^{-3}$), and interfacial area between the slag and metal, respectively. The symbols '*' and 'b' denote the interface and bulk phase, respectively, while the subscripts 's' and 'm' signify the slag and metal components.

In relation to reaction (1), a discernible correlation exists among the rates of reaction delineated by the concentrations of [S] and [O] within the molten steel, as well as the presence of (CaO) and (CaS) within the slag.

$$-\frac{dn_{[\text{O}]}}{dt} = -\frac{dn_{(\text{CaS})}}{dt} = \frac{dn_{(\text{CaO})}}{dt} = \frac{dn_{[\text{S}]}}{dt} \quad (6)$$

In accordance with the interconversion relationship between volumetric molar concentration and mass fraction $C_i = \frac{w[i]_{\%}}{100} \cdot \frac{\rho_m}{M_i}$ (mol · cm⁻³), and with the definition of volumetric molar concentration $C_i = \frac{n_i}{V}$ (mol · cm⁻³), Equation (7) is obtained.

$$\frac{dw[i]_{\%}}{dt} = \frac{A\rho_m k_i}{W_m} (w[i]_{\%}^* - w[i]_{\%}^b) \quad (7)$$

Utilizing Equation (6), the intricate relationships correlating the temporal evolution of $w(\text{CaO})_{\%}$ and $w(\text{CaS})_{\%}$ constituents within the slag, and $w[\text{S}]_{\%}$ in molten steel, are shown in Equations (8)–(10).

$$\frac{dw(\text{CaO})_{\%}}{dt} = \frac{W_m}{W_s} \frac{M_{\text{CaO}}}{M_S} \frac{dw[\text{S}]_{\%}}{dt} \quad (8)$$

$$\frac{dw(\text{CaS})_{\%}}{dt} = -\frac{W_m}{W_s} \frac{M_{\text{CaS}}}{M_S} \frac{dw[\text{S}]_{\%}}{dt} \quad (9)$$

$$\frac{dw[\text{O}]_{\%}}{dt} = -\frac{M_{\text{O}}}{M_S} \frac{dw[\text{S}]_{\%}}{dt} \quad (10)$$

with $Q_{\text{CaO}} = \frac{W_m}{W_s} \cdot \frac{M_{\text{CaO}}}{M_S}$, $Q_{\text{CaS}} = \frac{W_m}{W_s} \cdot \frac{M_{\text{CaS}}}{M_S}$ and $Q_{\text{O}} = \frac{M_{\text{O}}}{M_S}$, Equations (8)–(10) may be expressed as Equations (11)–(13), respectively.

$$\frac{dw[i]_{\%}}{dt} = \frac{A\rho_m k_i}{W_m} (w[i]_{\%}^* - w[i]_{\%}^b) \quad (11)$$

$$\frac{dw[i]_{\%}}{dt} = \frac{A\rho_m k_i}{W_m} (w[i]_{\%}^* - w[i]_{\%}^b) \quad (12)$$

$$\frac{dw[i]_{\%}}{dt} = \frac{A\rho_m k_i}{W_m} (w[i]_{\%}^* - w[i]_{\%}^b) \quad (13)$$

The concentration of sulfur at the slag–steel interface can be determined through the law of mass action. When the interfacial chemical reactions attain equilibrium, the activities of the constituents should conform to the law of mass action.

$$K_{[\text{S}]-[\text{O}]} = \frac{a_{\text{CaS}} a_{\text{O}}}{a_{\text{CaO}} a_{\text{S}}} = \frac{\left(\frac{2w(\text{S})_{\%}^* a_{\text{CaS}}}{M_S \sum n_i} \right) f_{\text{O}} w[\text{O}]_{\%}^*}{\gamma_{\text{CaO}} x_{\text{CaO}}^* f_{\text{S}} w[\text{S}]_{\%}^*} \quad (14)$$

where $a_{[i]}$ and f_i are the activity and activity coefficient of composition i in a metal referred to the 1% standard state, with mass percentage $w[i]_{\%}$ as the concentration unit (–) and a_i and γ_i are the activity and activity coefficient of composition i in the slag relative to pure matter as a standard state, with mole fraction x_i as the concentration unit (–).

The association between the molar ratio of a slag ingredient and its mass percentage is elucidated via $x_i = \frac{n_i}{\sum n_i} = \frac{m_i}{M_i \sum n_i}$.

Assuming a starting slag mass of 100 g in the IMCT modeling computations, the following equation can be used:

$$x_i = \frac{w(i)_{\%}}{M_i \sum n_i} \quad (15)$$

where M_i and T are the molar mass of composition i in slag (g · mol⁻¹) and absolute temperature (K), respectively, and $\sum n_i$ is the total mole number in 100 g of slag (mol).

Given the negligible variation in the compositions of the constituents in Equation (1), the activity coefficients of these components are considered to be approximately invariant throughout the reaction. Within the domain of isothermal thermodynamics, by integrating these coefficients $\frac{f_S \gamma_{\text{CaO}} M_{\text{CaS}}}{2f_{\text{O}} M_{\text{CaO}}}$ with the equilibrium constants intrinsic to chemical processes

and ascribing them as the effective equilibrium coefficient, symbolized as E_S , Equation (14) is obtained.

$$E_S = \frac{w(\text{CaS})_{\%}^* w[\text{O}]_{\%}^*}{w(\text{CaO})_{\%}^* w[\text{S}]_{\%}^*} = K_{[\text{S}]-[\text{O}]} \frac{f_S \gamma_{\text{CaO}} M_{\text{CaS}}}{2f_{\text{O}} M_{\text{CaO}}} \quad (16)$$

At this moment, the concentration of sulfur at the slag–steel interface can be expressed as follows: $w[\text{S}]_{\%}^* = \frac{w(\text{CaS})_{\%}^* w[\text{O}]_{\%}^*}{E_S w(\text{CaO})_{\%}^*}$.

$$w[\text{S}]_{\%}^* = \frac{w(\text{CaS})_{\%}^* w[\text{O}]_{\%}^*}{E_S w(\text{CaO})_{\%}^*} \quad (17)$$

Assuming that the mass transfer of sulfur is the rate-controlling step for the desulfurization reaction in molten steel, then $w(\text{CaO})_{\%}^* = w(\text{CaO})_{\%}^b$, $w[\text{O}]_{\%}^* = w[\text{O}]_{\%}^b$, $w(\text{CaO})_{\%}^* = w(\text{CaO})_{\%}^b$.

$$\frac{dw[\text{S}]_{\%}}{dt} = \frac{A\rho_m k_{S,m}}{W_m} (w[\text{S}]_{\%}^* - w[\text{S}]_{\%}) \quad (18)$$

Substituting Equation (17) into Equation (18) yields Equation (19).

$$-\frac{dw[\text{S}]_{\%}}{dt} = \frac{A\rho_m k_{S,m}}{W_m} \left(w[\text{S}]_{\%}^b - \frac{w(\text{CaS})_{\%}^b w[\text{O}]_{\%}^b}{E_S w(\text{CaO})_{\%}^b} \right) \quad (19)$$

Assuming an initial sulfur content in the molten steel of $w[\text{S}]_{\%}^0$, the sulfur content at a reaction time t is $w[\text{S}]_{\%}$. Consequently, the variation in the sulfur content within the molten steel can be determined by the difference between these two values, $\Delta w[\text{S}]_{\%} = w[\text{S}]_{\%}^0 - w[\text{S}]_{\%}$. Similarly, at instance t , the concentration of CaO in the slag is $w(\text{CaO})_{\%}$, the concentration of CaS is $w(\text{CaS})_{\%}$, and the concentration of O in the molten steel is $w[\text{O}]_{\%}$. Adhering to the principle of mass conservation and the stoichiometric relationships in reaction (1), all these concentrations can be expressed in terms of $w[\text{S}]_{\%}$, as elucidated in Equations (20)–(22).

$$w(\text{CaO})_{\%} = w(\text{CaO})_{\%}^0 + Q_{\text{CaO}} \Delta w[\text{S}]_{\%} \quad (20)$$

$$w(\text{CaS})_{\%} = w(\text{CaS})_{\%}^0 - Q_{\text{CaS}} \Delta w[\text{S}]_{\%} \quad (21)$$

$$w[\text{O}]_{\%} = w[\text{O}]_{\%}^0 - Q_{\text{O}} \Delta w[\text{S}]_{\%} \quad (22)$$

Upon substituting Equation (20) through (22) into Equation (19), Equation (23) is obtained.

$$\left(\frac{dw[\text{S}]_{\%}}{dt} \right) = \frac{A\rho_m k_{S,m}}{W_m} \left(\frac{\left(w(\text{CaS})_{\%}^0 - Q_{\text{CaS}} \Delta w[\text{S}]_{\%} \right) \left(w[\text{O}]_{\%}^0 - Q_{\text{O}} \Delta w[\text{S}]_{\%} \right)}{E_S \left(w(\text{CaO})_{\%}^0 + Q_{\text{CaO}} \Delta w[\text{S}]_{\%} \right)} - w[\text{S}]_{\%} \right) \quad (23)$$

The separation of variables from Equation (23) leads to the derivation of Equation (24).

$$\int_{w[\text{S}]_{\%}^0}^{w[\text{S}]_{\%}} \frac{dw[\text{S}]_{\%}}{\left(\frac{\left(w(\text{CaS})_{\%}^0 - Q_{\text{CaS}} \Delta w[\text{S}]_{\%} \right) \left(w[\text{O}]_{\%}^0 - Q_{\text{O}} \Delta w[\text{S}]_{\%} \right)}{E_S \left(w(\text{CaO})_{\%}^0 + Q_{\text{CaO}} \Delta w[\text{S}]_{\%} \right)} - w[\text{S}]_{\%} \right)} = \frac{A\rho_m k_{S,m}}{W_m} t \quad (24)$$

In accordance with a similar methodology, the mass transfer of CaS in the slag phase as the RCS is as follows:

$$\int_{w[\text{S}]_{\%}^0}^{w[\text{S}]_{\%}} \frac{Q_{\text{CaS}} dw[\text{S}]_{\%}}{\left(w(\text{CaS})_{\%}^0 - Q_{\text{CaS}} \Delta w[\text{S}]_{\%} \right) - \frac{E_S w[\text{S}]_{\%} \left(w(\text{CaO})_{\%}^0 + Q_{\text{CaO}} \Delta w[\text{S}]_{\%} \right)}{\left(w[\text{O}]_{\%}^0 - Q_{\text{O}} \Delta w[\text{S}]_{\%} \right)}} = \frac{A\rho_s k_{\text{CaS},s}}{W_s} t \quad (25)$$

The mass transfer of CaO in the slag phase as the RCS is as follows:

$$\int_{w[S]_0}^{w[S]_t} \frac{Q_{CaO} dw[S]_t}{\frac{(w[CaS]_0 - Q_{CaS} \Delta w[S]_t)(w[O]_0 - Q_O \Delta w[S]_t)}{E_S w[S]_t} - (w[CaO]_0 + Q_{CaO} \Delta w[S]_t)} = \frac{A \rho_s k_{CaO,s} t}{W_s} \quad (26)$$

The mass transfer of O in the molten steel phase as the RCS is as follows:

$$\int_{w[S]_0}^{w[S]_t} \frac{Q_O dw[S]_t}{\left(w[O]_0 - Q_O \Delta w[S]_t \right) - \frac{E_S (w[CaO]_0 + Q_{CaO} \Delta w[S]_t) w[S]_t}{(w[CaS]_0 - Q_{CaS} \Delta w[S]_t)}} = \frac{A \rho_m k_{O,m} t}{W_m} \quad (27)$$

Equation (24) through (27) can each be expounded as functions of the mass percentage of sulfur content within the molten steel. Their general formulation is shown in Equation (28):

$$F(w[S]_t) = f_i t \quad (28)$$

In instances where the mass transfer of [O] and [S] in the molten steel or the mass transfer of (CaO) and (CaS) in the slag become the rate-controlling steps of the desulfurization reaction, the correlation between $F(w[S]_t)$ and time is linear, with the slope f_i being constant. In the absence of such a scenario, the gradient f_i deviates from its constant nature. Theoretically, with Equation (24) through (27), a singular relationship linearly aligns with time variable t , thus signifying the validity of a sole RCS hypothesis. The pertinent diffusional coefficient k_i can be extrapolated from the deduced gradient.

4. Research Findings and Discussion

4.1. Experimental Results

Following the experimental scheme provided in Table 3, kinetic experiments were conducted using the apparatus shown in Figure 2. At a temperature of 1873 K, the SS-5Si molten steel interacted with nine different slags, each characterized by varying basicity, Al_2O_3 content, and CaF_2 content. The sulfur content in the molten steel was measured at intervals of 1, 5, 10, 15, and 30 min, and the results are listed in Table 4.

As elucidated in Table 4, the temporal variation in the sulfur content in the molten steel is evident. Notably, when the Al_2O_3 content in the slag remains beneath a threshold of 2.72%, the slag's basicity exerts the most pronounced influence on the sulfur content within the molten steel. Transitioning from a basicity of 1 to 2 results in a significant plunge in sulfur content, with a reduction from 11.3 ppm to 3.5 ppm within a span of 30 min. Conversely, upon elevating the basicity to 3, the content exhibits only a nominal decline to 2.2 ppm. Maintaining the alkalinity at 2 and concurrently either increasing the Al_2O_3 content from 2.04% to 9.61% or increasing the CaF_2 fraction from 20.87% to 31.62%, the oscillation in sulfur content at the 30 min mark remains negligible. Consequently, the data derived from experiments S1–S3 are instrumental in determining the pivotal, rate-controlling step of the desulfurization process.

4.2. Determination of the RCS in the Kinetics of the Desulfurization Reaction

4.2.1. Determination of the Slag Composition

By integrating the experimental findings from S1–S3 in Table 4 into Equations (24)–(27), Figure 4 is created. This figure shows the insertion of the measured sulfur content, determined at distinct intervals under varied basicity conditions, into the respective $F(w[S]_t)$ functional relationships derived from the four distinct assumptions regarding the mass transfer conditions as the predominant rate-controlling step (RCS) governing the kinetics of the desulfurization reaction. In the subsequent stage, through the graphical representation of the computed outcomes versus time, the verification for the four assumptions under the specified slag basicity conditions of S1, S2, and S3 can be derived. Based on observations,

at basicities of 1, 2, and 3, the deduction that the mass transfer of [S] within the molten steel operates as the RCS shows a progressive increase in the $F(w[S]_{\%})$ versus time graph. Conversely, the tendencies of the graphs corresponding to the mass transfer of [O] in the molten steel and (CaO) and (CaS) in the slag are nearly horizontal. Based on these observations, the deduction that [S] functions as the RCS within molten steel is accurate, while the three other deductions pertaining to [O], (CaO), and (CaS) acting as RCSs are not accurate. However, a broader experimental framework is needed to conclusively discern the dominant RCS.

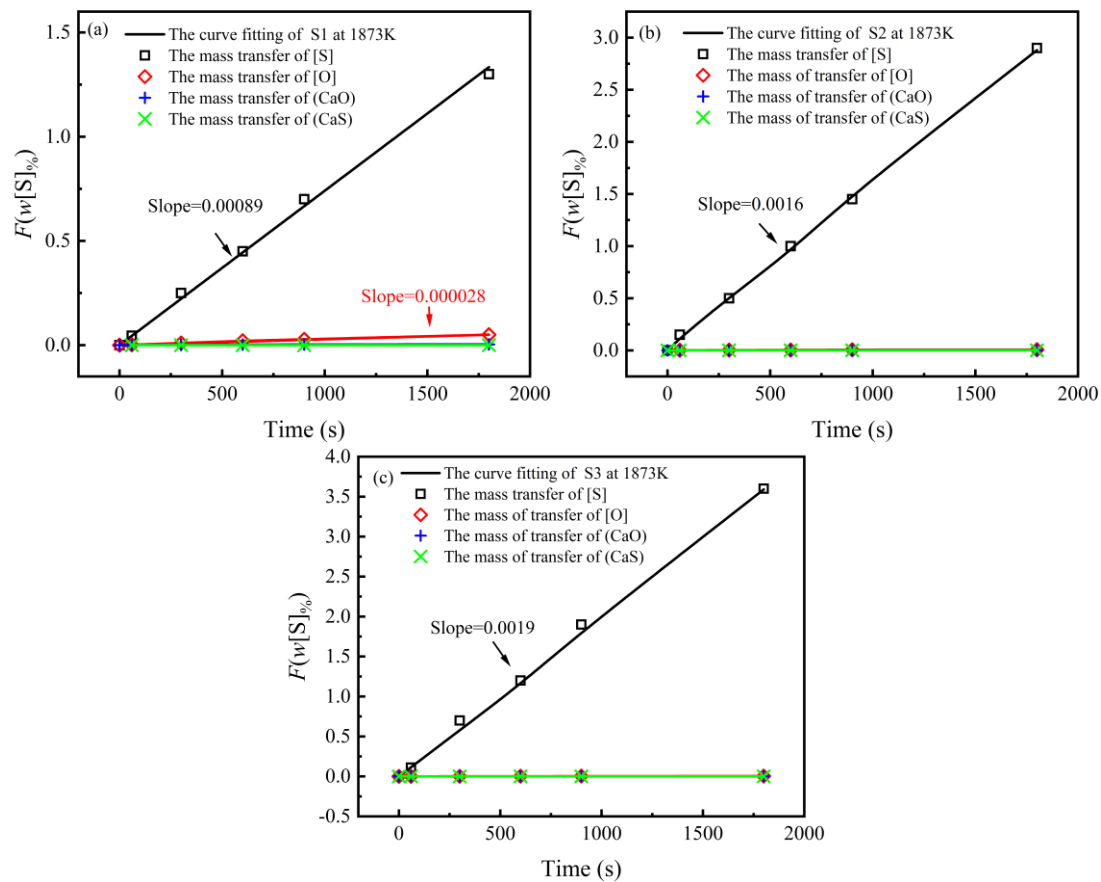


Figure 4. Determination of the mass transfer coefficient of S for the different slag basicities: (a) S1, (b) S2, (c) S3 at 1873 K (1600 °C).

Based on the findings, further investigation into the roles of Al_2O_3 and CaF_2 within the slag matrix and their impact on the RCS of the desulfurization reaction is needed. Similarly, considering the results on slag basicity's role in confirming the RCS of the desulfurization kinetics, experiments S4–S6 were designed with a fixed basicity of 2 and varying Al_2O_3 content, producing varied sulfur results over time. These results were mapped to the four RCS conditions from Equations (24)–(27), and calculated patterns for $F(w[S]_{\%})$ over time were obtained. Consequently, three distinct $F(w[S]_{\%})$ correlation graphs, corresponding to the S4–S6 experiments, were expected. These findings aligned with those in Figure 4, confirming the deduction that the mass transfer of sulfur in molten steel corresponds to the RCS. In contrast, other deductions for [O], (CaS), and (CaO) nearly approached zero. These experimental results are merged in Figure 5a. Similarly, experiments S7–S9, with a consistent basicity of 2 but varying CaF_2 , consistently supported that the mass transfer of sulfur was the RCS, as shown in Figure 5b.

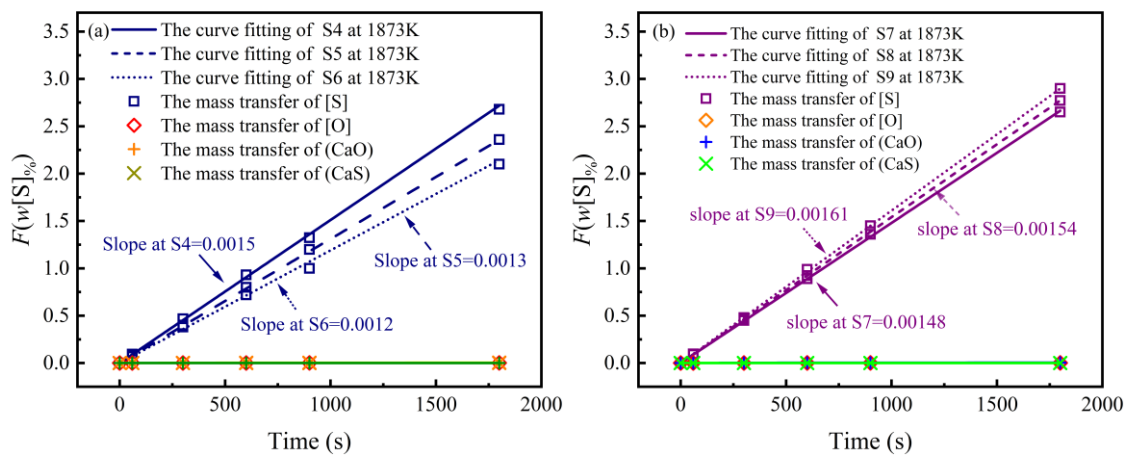


Figure 5. Determination of the mass transfer coefficient of S for the different slag compositions: (a) S4, S5, and S6; (b) S7, S8, and S9 at 1873 K (1600 °C).

In summary, the variations in the slag basicity spanning from 1–3 or at a basicity of 2 paired with calibrated adjustments in Al_2O_3 and CaF_2 provided the same results: the mass transfer of [S] is essential and acts as the RCS of desulfurization kinetics. Nonetheless, the influence of the variation in the experimental temperatures needs to undergo a more thorough exploration.

4.2.2. Determination of the System Temperature

To further determine the RCS of the desulfurization kinetics during the slag–steel reaction process, kinetic experiments were conducted under varying temperature conditions. Since the main factor affecting RCS in slag composition is the slag basicity, and the contents of Al_2O_3 and CaF_2 have no significant effect, experiments were carried out at temperatures of 1773 K, 1823 K, and 1873 K, selecting the S1 and S2 experimental schemes designed in Table 3 (with basicities $R = 1$ and 2), respectively. Six sets of kinetic experiments were performed, yielding experimental results for sulfur content in the steel at 1, 5, 10, 15, and 30 min, as shown in Tables 5 and 6.

Table 5. Sulfur content of S1 experimental ingots at different temperatures (ppm).

| Variable | 0 min | 1 min | 5 min | 10 min | 15 min | 30 min |
|----------|-------|-------|-------|--------|--------|--------|
| 1773 K | 22 | 21.4 | 19.2 | 17.3 | 15.5 | 12.6 |
| 1823 K | 22 | 20.7 | 18.1 | 15.7 | 14.0 | 11.8 |
| 1873 K | 22 | 18.9 | 16.4 | 13.7 | 12.4 | 11.3 |

Table 6. Sulfur content of S2 experimental ingots at different temperatures (ppm).

| Variable | 0 min | 1 min | 5 min | 10 min | 15 min | 30 min |
|----------|-------|-------|-------|--------|--------|--------|
| 1773 K | 22 | 14.5 | 10.8 | 7.9 | 5.0 | 4.1 |
| 1823 K | 22 | 14.3 | 10.6 | 7.5 | 4.5 | 3.5 |
| 1873 K | 22 | 13.7 | 10.3 | 7.2 | 4.2 | 3.2 |

Substituting the sulfur content in different molten steels into the four Equations (24)–(27) assumes that the mass transfer of [O], [S] in the molten steel and (CaO), and (CaS) in the slag is RCS. Similarly, the relationship curve between the sulfur content variable function $F(w[S]_{\%})$ and time was obtained, analogous to Figure 4. Thus, under the compositions of slags S1 and S2, at three different temperatures, it is also possible to draw 12 $(F(w[S]_{\%})-t)$ relation curves, as shown in Figure 6a,c. It is observable that in each graph, the slope of the curve $F(w[S]_{\%})-t$, which assumes mass transfer of [S] in the molten steel as the limiting step,

is positive. Conversely, the slopes of the curves corresponding to the other three assumptions are approximately zero. Therefore, the graphs made at the three temperatures are combined together. It should be noted that at a slag basicity of 1, the enlarged curves of RCS versus time, which are based on the mass transfer of [O] in the molten steel at different temperatures, also exhibit a positive slope, as shown in Figure 6b. The slope $f_i = A\rho_m k_{i,m}/W_m$ corresponds to the mass transfer of [i] in the liquid steel. Among these parameters, the equilibrium content of each component can be derived from thermodynamic equilibrium calculations. The density ρ (kg/m^3) of the molten steel and molten slag can be determined from the results of previous studies, and the reaction area A (m^2) can be obtained by calculating the diameter of the reaction crucible. By calculating when $R = 1$, the mass transfer coefficient of [O] in molten steel, $k_{O,m}$, is around $3.5 \times 10^{-7} \text{ m}\cdot\text{s}^{-1}$ at different temperatures, indicating a very low mass transfer rate. However, in our laboratory research on the deoxidation reaction of SS-5Si with $\text{CaF}_2\text{-CaO-Al}_2\text{O}_3\text{-MgO-SiO}_2$ slag, the mass transfer coefficient of [O] in molten steel was experimentally verified to be $4.0 \times 10^{-6} \text{ m}\cdot\text{s}^{-1}$ ($R = 1$). Jae Hong Shin et al. [49], Ren et al. [50], and Park et al. [51] also obtained values for $k_{O,m}$ under different steel types, slag composition, and other smelting conditions ranging from $1.0 \times 10^{-4} \text{ m}\cdot\text{s}^{-1}$ to $1.0 \times 10^{-6} \text{ m}\cdot\text{s}^{-1}$. In contrast, the assumption that mass transfer of [O] in molten steel under different temperatures is based on RCS does not hold.

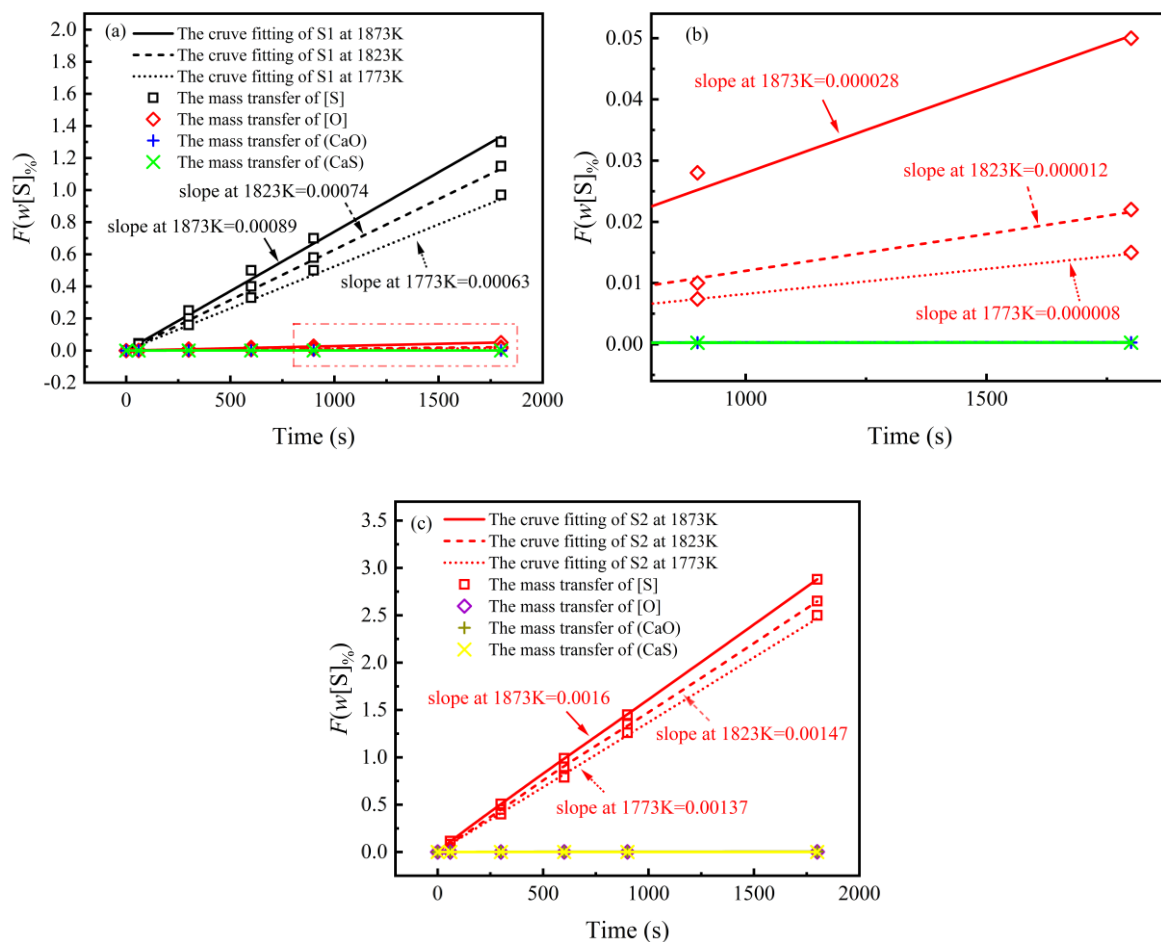


Figure 6. The relationship between $F(w[S]\%)$ and time at temperatures (1772, 1823, and 1873 K) under slag basicity: (a) S1; (b) Localized expansion diagram demarcated by the dotted line in (a); (c) S2.

In kinetic reaction processes, the temperature T influences both the diffusion coefficient D and the chemical reaction rate constant k , where $D = D_0 e^{-E_D/RT}$ and $k = Z_0 e^{-E/RT}$. Both D and k have an exponential relationship with the activation energy E ; E is the parameter gauging the magnitude of this temperature effect. In the realm of chemical processes, the activation energy, E , for chemical reactions is much higher than the activation energy for

diffusion, ED . Consequently, the influence of temperature, T , on the rate constant, k , is considerably more pronounced than its impact on the diffusion coefficient, D . The activation energy, ED , corresponding to diffusion-limited steps varies among different components in both molten steel and slag. Thus, accurately determining the apparent activation energy for desulfurization reactions is highly important. According to the Arrhenius equation [52], the relationship between the diffusion coefficient, D , or the mass transfer coefficient, k , and temperature, T , can be expressed by either Equation (29) or (30).

$$\ln(D/\delta) = \ln A - E_D/RT \quad (29)$$

$$\ln(k_{s,m}) = \ln A - E_D/RT \quad (30)$$

where k represents the reaction rate ($\text{m}\cdot\text{s}^{-1}$); A is a pre-exponential factor (dimensionless); E_D is the apparent activation energy ($\text{kJ}\cdot\text{mol}^{-1}$); R is the gas constant ($8.314 \text{ J}\cdot\text{mol}^{-1}\cdot\text{K}^{-1}$); and T is the absolute temperature (K).

According to Figure 6a–c, under the conditions of basicities of 1 and 2, and temperatures of 1773 K, 1823 K, and 1873 K, the mass transfer coefficient of sulfur in molten steel, $k_{s,m}$, can be determined. Subsequently, by establishing a linear relationship between $\ln(D/\delta)$ and $(1/T)$, the apparent activation energy value can be calculated, as listed in Table 7.

Table 7. The mass transfer coefficient of sulfur in SS-5Si steel at various temperatures under the alkalinities of 1 and 2.

| R | 1773 K | 1823 K | 1873 K | $E_D/(\text{kJ}\cdot\text{mol}^{-1})$ |
|---|-----------------------|-----------------------|-----------------------|---------------------------------------|
| 1 | 7.27×10^{-6} | 8.72×10^{-6} | 1.04×10^{-5} | 99.77 |
| 2 | 1.36×10^{-5} | 1.60×10^{-5} | 1.86×10^{-5} | 92.29 |

From Table 7, for SS-5Si steel during the deep desulfurization process, when the mass transfer of [S] in the molten steel is the RCS, the corresponding apparent activation energy has an average value at alkalinity levels of 1 and 2, as follows: $E_D = (E_{D,1} + E_{D,2})/2 = 96.03 \text{ kJ}\cdot\text{mol}^{-1}$.

Following thorough computations, the mass transfer of sulfur within molten steel acts as the RCS in the desulfurization reaction, showing distinct mass transfer coefficients of [S] in SS-5Si under varying alkalinity: $1.04 \times 10^{-5} \text{ m}\cdot\text{s}^{-1}$ ($R = 1$), $1.86 \times 10^{-5} \text{ m}\cdot\text{s}^{-1}$ ($R = 2$), and $2.24 \times 10^{-5} \text{ m}\cdot\text{s}^{-1}$ ($R = 3$). The influence of slag composition on desulfurization has been studied by some groups. TS Jeong et al. [53], in their seminal work, investigated the effects of diverse CaO/SiO₂ ratios and CaF₂ content in the CaO-SiO₂-CaF₂-Al₂O₃-MgO slag on the desulfurization behavior of 316L stainless steel at 1873 K. They expressed the overall mass transfer rate as a function of a particular variable: $\log C_{S^{2-}} - \log \eta$. Their results showed that when the slag basicity was less than 1.7, the desulfurization rate was jointly governed by the mass transfer of sulfur in the molten steel and CaS in the slag. However, when the basicity surpassed 1.7, the desulfurization was predominantly controlled by the mass transfer of sulfur within the molten steel, which was congruent with the conclusions drawn from our in-depth desulfurization studies of SS-5Si stainless steel at various basicity levels. JG Kang et al. [54] found that the overall mass transfer coefficient, which was determined through k_m and k_{sL} , defined the general desulfurization rate; the activation energy for the process was estimated to be 58.7 kJ/mol. The desulfurization of molten steel by using the CaO-SiO₂-CaF₂-Al₂O₃-MgO slag was customarily controlled by the mass transfer of [S] within the metallic phase. Roy et al. [55] introduced a kinetic model, articulating the influence of Si in molten steel on the desulfurization of Al-killed steel. They asserted that an increase in the Si content of the steel inhibited the reduction in Si and an increase in FeO/MnO reduced the consumption of Al; thus, more Al was able to participate in the desulfurization. Consequently, the desulfurization rate was controlled by the mass transfer of [S] within the molten steel, with a diffusion constant $k_{s,m}$ of approximately $1.1 \times 10^{-4} \text{ m}\cdot\text{s}^{-1}$, which correlated with the results from our desulfurization study. Nonethe-

less, due to the disparities in molten steel composition and slag constituents, the derived mass transfer coefficient of sulfur in our study slightly deviated from the extant literature. In summation, when the basicity exceeds 1 for the desulfurization of SS-5Si steel in conjunction with CaF_2 -CaO- Al_2O_3 -MgO- SiO_2 slag, the mass transfer of [S] within molten steel is the RCS in the kinetics of the desulfurization reaction.

The aforementioned research clearly ascertains that the diffusion of sulfur within molten steel is the limiting factor in the desulfurization reaction. Thus, within a slag basicity range of 1 to 3, when the slag contains Al_2O_3 levels of between 2.04% and 9.61% and CaF_2 levels from 20.8% to 31.62%, the kinetic model of the desulfurization reaction is represented by Equation (31).

$$\int_{w[\text{S}]_0}^{w[\text{S}]_t} \frac{dw[\text{S}]_t}{\frac{(w(\text{CaS})_0 - Q_{\text{CaS}}\Delta w[\text{S}]_t)(w(\text{O})_0 - Q_{\text{O}}\Delta w[\text{S}]_t)}{E_{\text{S}}(w(\text{CaO})_0 + Q_{\text{CaO}}\Delta w[\text{S}]_t)} - w[\text{S}]_t} = \frac{k_{\text{S,m}}A\rho_{\text{m}}}{W_{\text{m}}}t \quad (31)$$

4.3. Influence of the Slag Components on the Desulfurization Rate of SS-5Si Molten Steel

From the established desulfurization kinetic Equation (30), at 1873 K, integrating three sets of varying conditions S1~S9 into Equation (30) provides the relationship between the sulfur content in molten steel over time, under varying basicity, Al_2O_3 contents, and CaF_2 contents, juxtaposed with experimental data. As per the desulfurization kinetic rate Equation (30), the calculated variation in sulfur content within the molten steel over time (represented by solid lines) closely corresponds with the experimental results (denoted by solid dots), as illustrated in Figure 7.

Figure 7 depicts the desulfurization reaction kinetics at 1873 K between the five-component slag system of CaF_2 -CaO- Al_2O_3 -MgO- SiO_2 and SS-5Si molten steel. Equation (30) represents the kinetic model of desulfurization, where the mass transfer of sulfur in the molten steel is the RCS under varying slag conditions. The simulated values align well with the measured ones, though there remain issues warranting discussion.

From Figure 7a, at a basicity of 1, the calculated sulfur content in molten steel, from 1 min to 15 min, consistently exceeds the experimental results and slightly falls below the actual by the 30 min mark. When the basicity is 2, the model's prediction at 1 min is lower than the experimental value, equal to it at 5 min, and subsequently remains lower than it for the remaining timeframes. At a basicity level of 3, the model's estimates for both 1 and 5 min exceed the experimental values; however, its subsequent estimates are all lower than it, with the largest discrepancy at 30 min. These observations elucidate two key issues: First, despite assuming that sulfur mass transfer is the limiting step in the four proposed kinetic mass transfer processes, and that it theoretically represents the kinetic equation for desulfurization reactions, the theoretical equation still differs from the actual process when compared with empirical data for the three basicity levels. Initially, the model overestimates the sulfur content, but this trend reverses over time. Second, as slag basicity increases from 1 to 3, thermodynamic calculations show a drastic decline in molten steel sulfur content to less than 2 ppm, a value difficult to achieve in 30 min actual measurements, causing the model's prediction to be slightly understandable.

Figure 7b explores the influence on deep desulfurization kinetics when the Al_2O_3 content in the slag is increased from 2.04% to 9.61% at a basicity of 2. It becomes clear that as the concentration of Al_2O_3 (at 2.04%) is reduced, the kinetic model's simulated results align better with the experimental values, indicating that efforts to accelerate deep desulfurization by amplifying the Al_2O_3 concentration in slag are ineffective.

Figure 7c shows the impact on the deep desulfurization kinetics of increasing CaF_2 content in the slag from 20.87% to 31.23% at a basicity of 2. With an increase in CaF_2 content, the experimental sulfur content at 1 min is considerably lower than the value that the model predicts. Moreover, a higher CaF_2 content correlates to a greater deviation between the experimental and simulated sulfur content. However, as time progresses, the effects of escalating CaF_2 content become increasingly negligible. The results indicate that while a

surge in CaF_2 content can potentially influence the initial stages of deep desulfurization, its impact on the overall desulfurization process remains minimal.

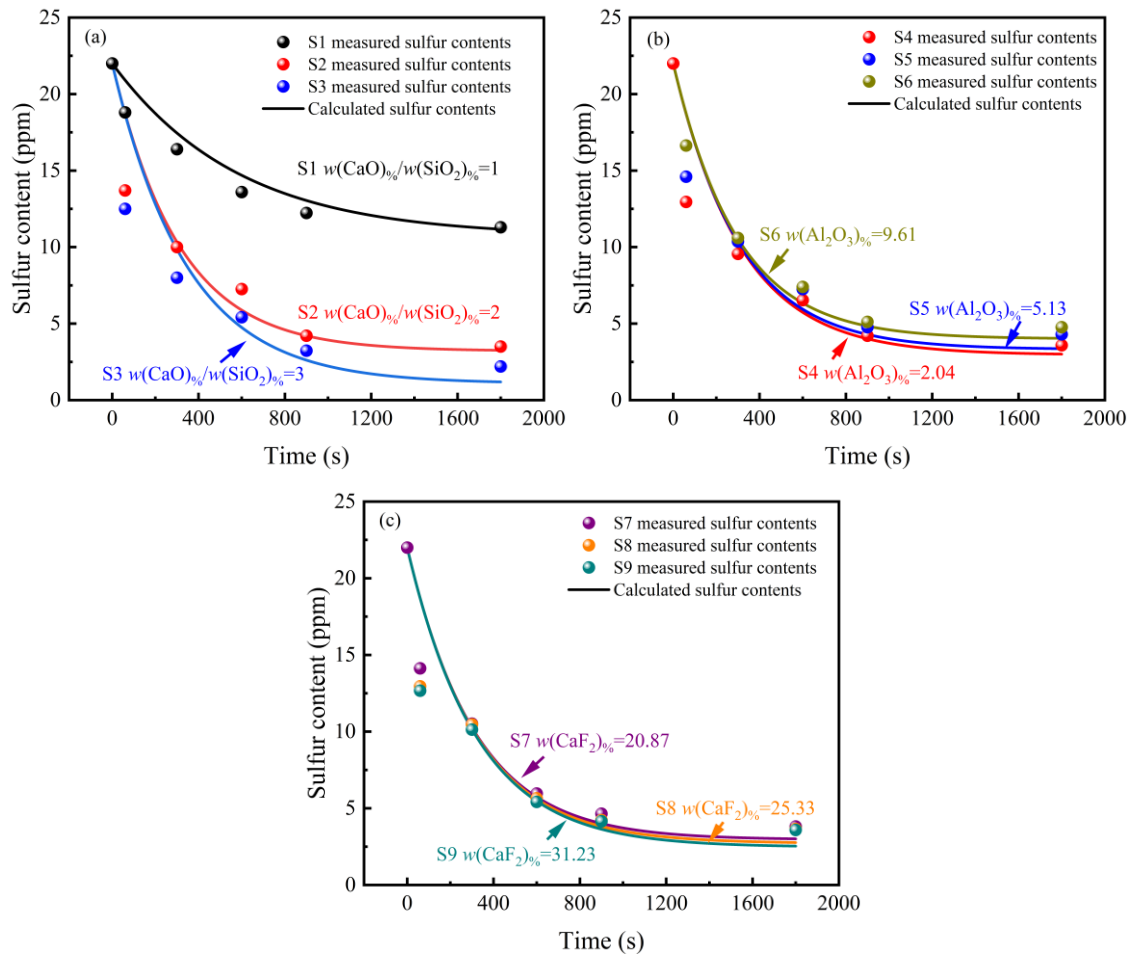


Figure 7. Model predictions (lines) and experimental data (points) of change in sulfur content with time for different slag compositions: (a) CaO, (b) Al_2O_3 , and (c) CaF_2 .

5. Conclusions

Utilizing the foundation equations of multiphase reaction kinetics within the paradigm of the established boundary layer theory, we thoroughly extrapolated the intricate desulfurization tendencies of CaF_2 -CaO- Al_2O_3 -MgO-SiO₂ slag in conjunction with 5 wt% high-silicon austenitic stainless steel (SS-5Si) via theoretical elucidation and our laboratory investigations. The main conclusions were as follows:

1. Based on the kinetic principle that a distinct mass transfer process exhibits the predominant rate-controlling mechanism, a comprehensive study of the slag basicity effects (spanning 1–3), Al_2O_3 content (ranging from 2.04–9.61%), CaF_2 content (ranging from 20.8–31.62%), and thermal conditions (at 1773 K, 1823 K, and 1873 K) were performed on the desulfurization kinetics of SS-5Si. Merging data from the nine experimental sets S1–S9 over varying intervals (1, 5, 10, 15, and 30 min), a thorough juxtaposition emerged between the quantified sulfur content in molten steel and the posited theoretical framework. The mass transfer of sulfur within the molten steel was the rate-controlling step for the $(\text{CaO}) + [\text{S}] = (\text{CaS}) + [\text{O}]$ reaction with the rate dynamics aligning coherently with the kinetic model
$$\int_{w[\text{S}]_0}^{w[\text{S}]_t} \frac{dw[\text{S}]_t}{(w[\text{CaS}]_0 - Q_{\text{CaS}} \Delta w[\text{S}]_t)(w[\text{O}]_0 - Q_{\text{O}} \Delta w[\text{S}]_t) - w[\text{S}]_t} = \frac{k_{\text{S,m}} A \rho_{\text{m}}}{W_{\text{m}}} t.$$
 At a thermal

point of 1873 K, the variation in the mass transfer coefficient of sulfur, $k_{\text{S,m}}$, in the molten

matrix was between $1.04 \times 10^{-5} \text{ m}\cdot\text{s}^{-1}$ and $2.24 \times 10^{-5} \text{ m}\cdot\text{s}^{-1}$, with an extrapolated desulfurization activation energy of 96.03 kJ/mol in this regime.

- Regarding the slag composition, the basicity R exerted the most influence on deep desulfurization. When the alkalinity was at 1, the sulfur content in the molten steel was reduced from 22 ppm to 11 ppm within a span of 30 min. However, when the alkalinity was increased to 3, over the same 30 min interval, the sulfur content was significantly reduced to 2.2 ppm. Within a range of 2.04% to 9.61% for Al_2O_3 and 20.8% to 31.62% for CaF_2 , a relatively lower Al_2O_3 content and higher CaF_2 content slightly increased the desulfurization rate during the initial phase within 5 min. Subsequently, these contents minimally influenced the kinetic behavior of the desulfurization process.

Author Contributions: Conceptualization, G.D. and H.G.; methodology, G.D. and H.G.; software, G.D. and X.P.; validation, G.D. and X.P.; formal analysis, G.D. and J.G.; investigation, G.D. and H.G.; data curation, G.D. and H.G.; writing—original draft preparation, G.D. and H.G. All authors have read and agreed to the published version of the manuscript.

Funding: This research received no external funding.

Data Availability Statement: The datasets used and/or analyzed during the current study are available from the corresponding author on reasonable request.

Conflicts of Interest: We declare that none of the authors have any financial or scientific conflicts of interest with regard to the research described in this manuscript.

References

- Chen, S.; Liang, T.; Zhou, Y.; Xing, W.; Zheng, C.; Ma, Y.; Wu, J.; Li, G.; Liu, K. Phase characterization and formation behavior in 6 wt% Si high-silicon austenitic stainless steel during isothermal aging. *Acta Metall. Sin. (Engl. Lett.)* **2021**, *34*, 649–656. [\[CrossRef\]](#)
- Kubo, S.; Futakawa, M.; Ioka, I.; Onuki, K.; Yamaguchi, A. Corrosion resistance of structural materials in high-temperature aqueous sulfuric acids in thermochemical water-splitting iodine–sulfur process. *Int. J. Hydrog. Energy* **2013**, *38*, 6577–6585. [\[CrossRef\]](#)
- Louie, D.K. *Handbook of Sulphuric Acid Manufacturing*; DKL Engineering Thornhill, Ont.: Thornhill, ON, Canada, 2005.
- Paul, A.; Elmrbet, S.; Alves, L.C.; da Silva, M.F.; Soares, J.C.; Odriozola, J.A. Ion microprobe study of the scale formed during high temperature oxidation of high silicon EN-1.4301 stainless steel. *Nucl. Instrum. Methods Phys. Res. Sect. B Beam Interact. Mater. At.* **2001**, *181*, 394–398. [\[CrossRef\]](#)
- Patel, M.; Vaidyanathan, R.M. Corrosion Behaviour of Sintered 316L Austenitic Stainless Steel Composites. *J. Mech. Eng. Technol.* **2014**, *5*, 121–128.
- Wijk, O.; Brabie, V. The Purity of Ferrosilicon and Its Influence on Inclusion Cleanliness of Steel. *ISIJ Int.* **1996**, *36*, S132–S135. [\[CrossRef\]](#)
- Sjöqvist, T.; Jönsson, P.; Grong, Ö. Inclusions in commercial low and medium carbon ferromanganese. *Metall. Mater. Trans. A* **2001**, *32*, 1049–1056. [\[CrossRef\]](#)
- Vasconcellos da Costa e Silva, A.L. Non-metallic inclusions in steels—origin and control. *J. Mater. Res. Technol. Jmrt* **2018**, *7*, 283–299. [\[CrossRef\]](#)
- Sun, Y.; Hebert, R.J.; Aindow, M. Non-metallic inclusions in 17-4PH stainless steel parts produced by selective laser melting. *Mater. Des.* **2018**, *140*, 153–162. [\[CrossRef\]](#)
- Choi, N.; Lim, K.R.; Na, Y.S.; Glatzel, U.; Park, J.H. Characterization of non-metallic inclusions and their influence on the mechanical properties of a FCC single-phase high-entropy alloy. *J. Alloys Compd.* **2018**, *763*, 546–557. [\[CrossRef\]](#)
- Park, J.; Kang, Y.B. Inclusions in Stainless Steels—A Review. *Steel Res. Int.* **2017**, *88*, 1700130. [\[CrossRef\]](#)
- Zerbst, U.; Madia, M.; Klinger, C.; Bettge, D.; Murakami, Y. Defects as a root cause of fatigue failure of metallic components. II: Non-metallic inclusions. *Eng. Fail. Anal.* **2019**, *98*, 228–239. [\[CrossRef\]](#)
- Ånmark, N.; Karasev, A.; Jönsson, P. The Effect of Different Non-Metallic Inclusions on the Machinability of Steels. *Materials* **2015**, *8*, 751–783. [\[CrossRef\]](#) [\[PubMed\]](#)
- Zhang, W.; Ji, H.; Ma, T.; Liu, Y.; Fan, J.; Fan, Z. Corrosion behaviors of 15% SiC p/2009Al composite in 3.5% NaCl solution. *Chin. J. Rare Met.* **2018**, *42*, 516.
- Liu, C.; Revilla, R.I.; Zhang, D.; Liu, Z.; Lutz, A.; Zhang, F.; Zhao, T.; Ma, H.; Li, X.; Terryn, H. Role of Al_2O_3 inclusions on the localized corrosion of Q460NH weathering steel in marine environment. *Corros. Sci.* **2018**, *138*, 96–104. [\[CrossRef\]](#)
- Shibaeva, T.V.; Laurinavichyute, V.K.; Tsirlina, G.A.; Arsenkin, A.M.; Grigorovich, K.V. The effect of microstructure and non-metallic inclusions on corrosion behavior of low carbon steel in chloride containing solutions. *Corros. Sci.* **2014**, *80*, 299–308. [\[CrossRef\]](#)

17. Dexiang, C.; Shaoming, Q. Influence of sulfur on inclusion and pitting resistance of 316L stainless steel. *Baosteel Tech. Res.* **2020**, *14*, 31–38.
18. Li, D.; Zhi, H.; Lai, Z.; Jin, Y. Localized Corrosion of Stainless Steel Triggered by Typical Inclusions in NaCl Solution: Oxy-Sulfide and MnS. *Materials* **2023**, *16*, 4323. [[CrossRef](#)]
19. Wilde, B.E.; Armijo, J.S. Influence of Sulfur on the Corrosion Resistance of Austenitic Stainless Steel. *Corrosion* **1967**, *23*, 208–214. [[CrossRef](#)]
20. Wan, Y.; Gao, S.; Zhang, X.; Tang, C.; Li, J.; Wen, Y. Effect of Manganese Sulfide Inclusion Morphology on the Corrosion Resistance and Pitting Corrosion Behavior of Free-Cutting Austenitic Stainless Steel. *J. Mater. Eng. Perform.* **2023**, *33*, 336–347. [[CrossRef](#)]
21. Alnajjar, M.; Christien, F.; Barnier, V.; Bosch, C.; Wolski, K.; Fortes, A.D.; Telling, M. Influence of microstructure and manganese sulfides on corrosion resistance of selective laser melted 17-4 PH stainless steel in acidic chloride medium. *Corros. Sci.* **2020**, *168*, 108585. [[CrossRef](#)]
22. Wagner, C.; Elliott, J. *The Physical Chemistry of Steelmaking*; Elliott, J.F., Ed.; Wiley: New York, NY, USA, 1958.
23. Zhang, J.; Schneider, A.; Inden, G. Characterisation of the coke formed during metal dusting of iron in CO–H₂–H₂O gas mixtures. *Corros. Sci.* **2003**, *45*, 1329–1341. [[CrossRef](#)]
24. Lin, Y.; Yi, Y.; Fang, M.; Ma, W.; Liu, W. Prediction model for SiO₂ activity in the CaO–Al₂O₃–SiO₂–MgO quaternary slag system. *Minerals* **2023**, *13*, 509. [[CrossRef](#)]
25. Nilsson, R.; Sichen, D.; Seetharaman, S. Estimation of sulphide capacities of multi-component silicate melts. *Scand. J. Metall.* **1996**, *25*, 128–134.
26. Sosinsky, N.J.; Sommerville, I. The composition and temperature dependence of the sulfide capacity of metallurgical slags. *Metall. Trans. B* **1986**, *17*, 331–337. [[CrossRef](#)]
27. Zhou, Q.; Li, Z.; Wei, Z.-S.; Wu, D.; Li, J.-Y.; Shao, Z.-Y. Microstructural features and precipitation behavior of Ti, Nb and V microalloyed steel during isothermal processing. *J. Iron Steel Res. Int.* **2019**, *26*, 102–111. [[CrossRef](#)]
28. Yan, P.; Huang, S.; Pandelaers, L.; Van Dyck, J.; Guo, M.; Blanpain, B. Effect of the CaO–Al₂O₃-Based top slag on the cleanliness of stainless steel during secondary metallurgy. *Metall. Mater. Trans. B* **2013**, *44*, 1105–1119. [[CrossRef](#)]
29. Ren, Z.-s.; Hu, X.-j.; Chou, K.-c. Calculation and analysis of sulfide capacities for CaO–Al₂O₃–SiO₂–MgO–TiO₂ slags. *J. Iron Steel Res. Int.* **2013**, *20*, 21–25. [[CrossRef](#)]
30. Nzotta, M.; Andreasson, M.; Jönsson, P.; Seetharaman, S. A study on the sulphide capacities of steelmaking slags. *Scand. J. Metall.* **2000**, *29*, 177–184. [[CrossRef](#)]
31. Hao, X.; Wang, X. A New Sulfide Capacity Model for CaO–Al₂O₃–SiO₂–MgO Slags Based on Corrected Optical Basicity. *Steel Res. Int.* **2016**, *87*, 359–363. [[CrossRef](#)]
32. Li, X.; Kang, Y.; Wu, G.; Xiao, A. Original position statistic distribution analysis for thin slab produced by CSP. *J. Iron Steel Res* **2009**, *21*, 9–12.
33. Wang, C.; Lu, Q.; Zhang, S.; Li, F. Study on sulphide capacity of CaO–SiO₂–Al₂O₃–MgO–FeO slags. *J. Univ. Sci. Technol. Beijing Miner. Metall. Mater.* **2006**, *13*, 213–217. [[CrossRef](#)]
34. Lv, W.; Xie, Z.; Mao, Z.; Yuan, P.; Jia, M. Hybrid modelling for real-time prediction of the sulphur content during ladle furnace steel refining with embedding prior knowledge. *Neural Comput. Appl.* **2014**, *25*, 1125–1136. [[CrossRef](#)]
35. Dou, G.; Guo, H.; Guo, J.; Li, S.; Yan, Y.; Wang, Z. Investigation of deoxidation of high-silicon austenitic sulfuric acid-resistant stainless steel. *Front. Mater.* **2022**, *9*, 937288. [[CrossRef](#)]
36. Eklund, G.S. Initiation of pitting at sulfide inclusions in stainless steel. *J. Electrochem. Soc.* **1974**, *121*, 467. [[CrossRef](#)]
37. Bigelow, L.; Flemings, M. Sulfide inclusions in steel. *Metall. Trans. B* **1975**, *6*, 275–283. [[CrossRef](#)]
38. Ban-Ya, S.; Hobo, M.; Kaji, T.; Itoh, T.; Hino, M. Sulphide capacity and sulphur solubility in CaO–Al₂O₃ and CaO–Al₂O₃–CaF₂ slags. *ISIJ Int.* **2004**, *44*, 1810–1816. [[CrossRef](#)]
39. Shankar, A. Sulphur partition between hot metal and high alumina blast furnace slag. *Ironmak. Steelmak.* **2006**, *33*, 413–418. [[CrossRef](#)]
40. Young, R.; Duffy, J.; Hassall, G.; Xu, Z. Use of optical basicity concept for determining phosphorus and sulphur slag-metal partitions. *Ironmak. Steelmak.* **1992**, *19*, 201–219.
41. Shim, J.-D.; BAN-YA, S. The Distribution of Oxygen between Liquid Iron and FeO–SiO₂–CaO–MgO Slags Saturated with MgO. *Tetsu-to-Hagané* **1981**, *67*, 1745–1754. [[CrossRef](#)]
42. Yang, X.-M.; Jiao, J.-S.; Ding, R.-C.; Shi, C.-B.; Guo, H.-J. A Thermodynamic Model for Calculating Sulphur Distribution Ratio between CaO–SiO₂–MgO–Al₂O₃ Ironmaking Slags and Carbon Saturated Hot Metal Based on the Ion and Molecule Coexistence Theory. *ISIJ Int.* **2009**, *49*, 1828–1837. [[CrossRef](#)]
43. Shi, C.-B.; Yang, X.-M.; Jiao, J.-S.; Li, C.; Guo, H.-J. A Sulphide Capacity Prediction Model of CaO–SiO₂–MgO–Al₂O₃ Ironmaking Slags Based on the Ion and Molecule Coexistence Theory. *ISIJ Int.* **2010**, *50*, 1362–1372. [[CrossRef](#)]
44. Duan, S.C.; Guo, X.L.; Guo, H.J.; Guo, J. A manganese distribution prediction model for CaO–SiO₂–FeO–MgO–MnO–Al₂O₃ slags based on IMCT. *Ironmak. Steelmak.* **2016**, *44*, 168–184. [[CrossRef](#)]
45. Hino, M.; Ito, K. *Thermodynamic Data for Steelmaking*; Tohoku University Press: Sendai, Japan, 2010.
46. Zhang, H.; Peng, Y.; Zhang, S.; Liu, C.; Cheng, R.; Ni, H. Effects of Refining Slag on Transformation and Removal of Inclusions in Type 430 Stainless Steel. *Metall. Mater. Trans. B* **2022**, *53*, 702–715. [[CrossRef](#)]

47. Robison, J.W.; Pehlke, R.D. Kinetics of chromium oxide reduction from a basic steelmaking slag by silicon dissolved in liquid iron. *Metall. Trans.* **1974**, *5*, 1041–1051. [[CrossRef](#)]
48. Pomfret, R.; Grievson, P. The kinetics of slag-metal reactions. *Can. Metall. Q.* **1983**, *22*, 287–299. [[CrossRef](#)]
49. Shin, J.H.; Chung, Y.; Park, J.H. Refractory–slag–metal–inclusion multiphase reactions modeling using computational thermodynamics: Kinetic model for prediction of inclusion evolution in molten steel. *Metall. Mater. Trans. B* **2017**, *48*, 46–59. [[CrossRef](#)]
50. Ren, Y.; Zhang, L.-F.; Zhang, Y. Modeling reoxidation behavior of Al–Ti-containing steels by CaO–Al₂O₃–MgO–SiO₂ slag. *J. Iron Steel Res. Int.* **2018**, *25*, 146–156. [[CrossRef](#)]
51. Park, D.-C.; Jung, I.-H.; Rhee, P.C.; Lee, H.-G. Reoxidation of Al–Ti containing steels by CaO–Al₂O₃–MgO–SiO₂ slag. *ISIJ Int.* **2004**, *44*, 1669–1678. [[CrossRef](#)]
52. Guo, H. *Metallurgical Physical Chemistry*; Metallurgical Industry Press: Beijing, China, 2006.
53. Jeong, T.S.; Cho, J.H.; Heo, J.H.; Park, J.H. Desulfurization behavior of Si-killed 316L stainless steel melt by CaO–SiO₂–CaF₂–Al₂O₃–MgO slag. *J. Mater. Res. Technol.* **2022**, *18*, 2250–2260. [[CrossRef](#)]
54. Kang, J.G.; Shin, J.H.; Chung, Y.; Park, J.H. Effect of slag chemistry on the desulfurization kinetics in secondary refining processes. *Metall. Mater. Trans. B* **2017**, *48*, 2123–2135. [[CrossRef](#)]
55. Roy, D.; Pistorius, P.C.; Fruehan, R.J. Effect of silicon on the desulfurization of Al-killed steels: Part II. Experimental results and plant trials. *Metall. Mater. Trans. B* **2013**, *44*, 1095–1104. [[CrossRef](#)]

Disclaimer/Publisher’s Note: The statements, opinions and data contained in all publications are solely those of the individual author(s) and contributor(s) and not of MDPI and/or the editor(s). MDPI and/or the editor(s) disclaim responsibility for any injury to people or property resulting from any ideas, methods, instructions or products referred to in the content.